Nanoscale

Accepted Manuscript

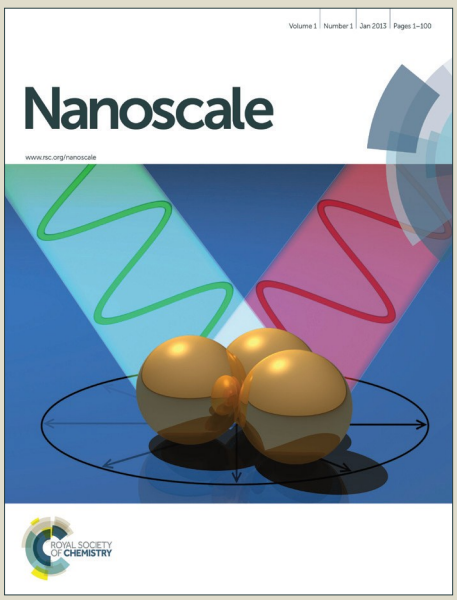

ROYAL SOCIETY OF CHEMISTRY

www.rsc.org/nanoscale

Zinc Oxide Nanoring Embedded Lacey Graphene Nanoribbons in Symmetric/Asymmetric Electrochemical Capacitive Energy Storage

Vikrant Sahu, Shubhra Goel, Raj Kishore Sharma* and Gurmeet Singh**

Department of Chemistry, University of Delhi, Delhi-110007, INDIA

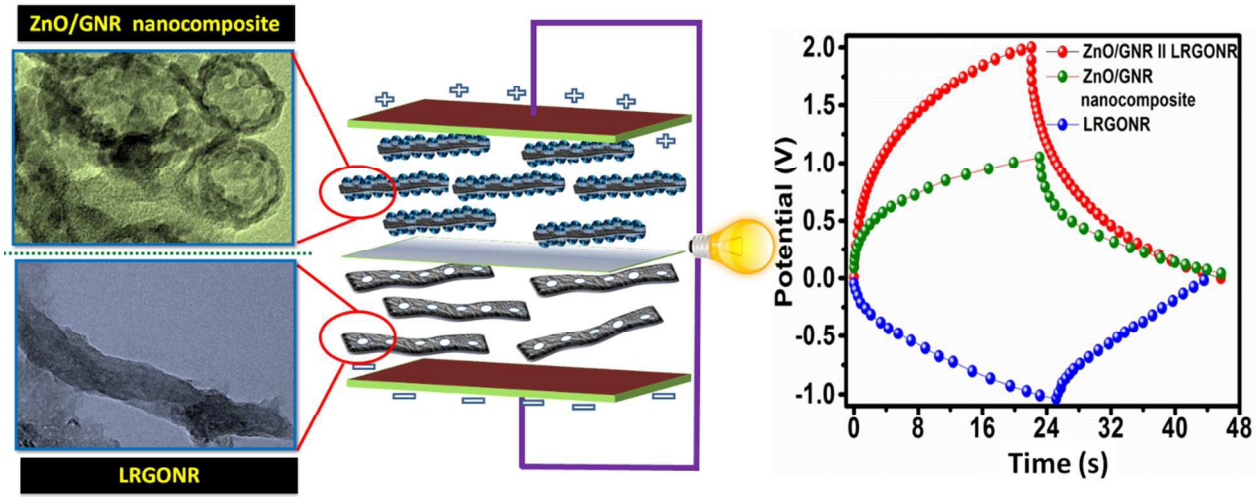

---

*Corresponding author : Raj K. Sharma
E-mail: drrajksharma@yahoo.co.in
**Co-corresponding author : Gurmeet Singh
E-mail: gurmeet123@yahoo.co.in
Tel. No. : +91-11-27666616

ABSTRACT

This article describes the synthesis and characterization of ZnO nanoring embedded graphene nanoribbons. Patterned holes (mesopore dia.) in graphene nanoribbons are chemically generated leading to high density of edge planes. These planes carry negatively charged surface groups (like -COOH, -OH) and therefore anchor the metal ions in a cordial fashion forming a string of metal ions along the edge planes. These strings of imbibed metal ions precipitate as tiny ZnO nanorings over lacey graphene nanoribbon. So obtained graphene nanoribbon (GNR) based hierarchical ZnO mesoporous structures are three dimensionally accessible to the electrolyte and demonstrate high performance in capacitive energy storage. The ZnO/GNR nanocomposite electrode in asymmetric supercapacitor device with lacey reduced graphene oxide nanoribbon (LRGONR) as negative electrode exhibit 2.0 V potential window in aqueous electrolyte and ultra short time constant (0.08s). The wide potential window consequently increased the energy density from 6.8 Wh kg^{-1} (ZnO/GNR symmetric) to 9.4 Wh kg^{-1} (ZnO/GNR‖LRGONR asymmetric). The relaxation time constant obtained for the asymmetric supercapacitor device was three order less compared to the ZnO (symmetric, 33s) supercapacitor device. High cycling stability of ZnO/GNR‖LRGONR up to 96.7 % capacitance retention, after 5000 GCD cycle at 2 mA cm^{-2} pave their way to a high performance aqueous electrochemical supercapacitive energy storage.

Key words: zinc oxide nanoring; graphene nanoribbon; asymmetric supercapacitor

1. INTRODUCTION

Recently, *graphene* is being reported as a proficient substrate for growing polymers/transition metal oxides in development of supercapacitor devices.[1] Its two-dimensional arrangement accounts for excellent energy storage due to large surface area, exceptional conductivity, carrier mobility, good mechanical strength, and high electrochemical stability.[2-8] The structural organizations arising from coupling of graphenes with polymers and/or metal oxides result in swift flow of electrolytic ions together with high electrical integrity through the porous conducting matrix.[9,10] A number of reports are available that discuss fabrication of efficient supercapacitors based on graphene nanocomposites with conducting polymers (e.g. polyaniline, polypyrrole etc.) and transition metal oxides (e.g. MnO_2, V_2O_5, SnO_2, ZnO, CuO_2, $Ni(OH)_2$, RuO_2 etc.) applying suitable approaches.[11-16] Inclusion of the *pseudocapacitive materials* with graphene that primarily constitute electrical double layer charge, enhance the overall capacitance and the energy density of supercapacitor electrodes.[17] Graphene based nanocomposite electrodes display beneficial properties like decreased agglomeration of metal oxide, complete orientation of the particles over support and improved electronic conduction. On the other hand presence of metal oxide particles over graphene restrains the re-stacking which in turn results in high electrolytic accessibility of the metal oxide and the underlying graphene. Such sandwiched and highly accessible structures are ideal for high capacitance, high energy and power density with good rate capability and cycling life.[10]

In contrast, graphene/metal oxide combinations have generally demonstrated an efficient positive electrode to work best in 0.0V to 1.0V range. The energy and power densities of the supercapacitor device with such positive electrode can be further increased by involving various

carbon allotropes like graphene, carbon nanotubes, activated carbon etc. as negative electrode. In the earlier reports, above combination is effectively and efficiently used.[18]

Among the different transition metal oxides, ZnO has lately emerged as an excellent pseudocapacitive material due to low cost, non-toxic, facile growth, abundance and eco-friendly nature.[19,20] It is widely known for its use in technological areas like catalysis, optoelectronics, photocatalysis, gas sensors, diodes, electroluminescence, flat display devices, piezoelectrics and so on due to attractive physical and chemical properties.[21] Enormous literature is available that confer synthesis of ZnO nanoparticles through different processes for instance microwave assisted ZnO growth,[22] precipitation,[23] sonochemical,[24] hydrothermal[25] etc. However, the development of ZnO/graphene based supercapacitors is still in infancy and the full utilization of ZnO as an efficient electrode is yet to be realized. Fabrication of ZnO/graphene nanocomposites has been explored by few researchers, wherein ZnO nanoparticles are embedded in graphene sheets for supercapacitor electrodes.[26-28] In contrast to graphene sheets, graphene nanoribbons (GNRs) exhibit superior properties owing to small size, relatively better conduction, low stacking and higher edge-density with increased nucleation-sites for metal oxides.[18,29] Considering the ongoing inclination of research towards *graphenes*, development of high-performance supercapacitors based on ZnO/graphene nanocomposites for advanced technological devices is therefore stimulating.[30-32]

In the outlined manuscript, synthesis of ZnO/GNR novel hybrid supercapacitor electrode material is discussed in which ZnO nanorings are anchored with the help of surface groups present at the edge planes of the lacey graphene oxide nanoribbon (LGONR). Electrochemical properties of the above nanostructured electrodes significantly improved compared to the pure

ZnO electrode. ZnO in general, build up as large rods or spherical structures which reduce electrolytic accessibility and the charge collection. Herein, for the first time we demonstrate an in-situ approach to develop ZnO particles over GNR *as tiny ring-shaped structures* due to substrate-assisted phenomenon. The method employed to synthesize GNR by chemical unzipping of MWCNTs is a modified version of the formerly reported synthesis route adopted by *J. Tour* and coworkers.[33] The uniqueness of our synthesis procedure is the creation of holes/lacey pattern in the GNR structures, described previously at-length by *V. Sahu et al*.[29] Different from the earlier works on ZnO/graphene nanocomposites, the prime focus of undertaken work is to highlight the significance of functionalities on edge planes of GNRs in initiating and arresting the growth of ZnO nanoparticles, without involving any additives/surfactants/capping agents or sophisticated techniques. The supercapacitor device characteristics of ZnO/GNR films explored in asymmetric/symmetric designs reveal high energy density and capacitive performance. The described synergistic effect of GNR and ZnO enhance the charge storage due to interconnected nanodimensional ZnO firmly adsorbed over lacey GNR. To the best of our knowledge, no such type of report based on fabrication of novel ZnO/GNR nanocomposite with exceptionally high performance has been described so far.

2. EXPERIMENTAL SECTION

2.1 Synthesis Procedures

2.1.1 Synthesis of LGONR and LRGONR

The LGONR was synthesized by chemical unzipping of MWCNTs as discussed in our previous articles.[29] 3.0 g of MWCNTs was added to 400 ml solution of H_2SO_4/H_3PO_4 and stirred for 1 hr till homogeneity was obtained. Subsequently, 18 g of $KMnO_4$ was gradually added to the above reaction mixture with constant stirring. Temperature of the mixture was maintained at 80^oC and

set on stirring for 12 hrs. The final product obtained is dried under vacuum and named as LGONR. Lacey reduced graphene oxide nanoribbon (LRGONR) was synthesized by reducing the LGONR in the KOH solution (6w/w %) at high temperature (600 ^{o}C) for 1 hr in the Argon. The detailed procedure is reported elsewhere.[29]

2.1.2 Synthesis of ZnO/GNR Nanocomposite

ZnO/GNR nanocomposite was synthesized using a co-precipitation method followed by heat treatment as shown in the schematic in Fig. 1. In a typical growth experiment, 400 mg LGONR was sonicated in 400 ml of deionized (DI) water until no traces of sediments appear. 6.25 ml of 1M $Zn(NO_3)_2.6H_2O$ was then added in the dispersed LGONR along with 6.4 ml of 1M $(NH_4)_2CO_3$ and the mixture was set on stirring for 2 hrs. Concurrently, 4 ml of liquid NH_3 was slowly added into the reaction mixture. After the completion of reaction, the greyish-black precipitate was filtered through 0.45µm PTFE membrane and thoroughly washed with DI water till the filtrate became neutral in pH. The filtrate was then dried and the coarse powder so obtained was annealed at 250^{o}C for 5 hrs to convert $ZnCO_3$ into ZnO. These chemical processes involved in the synthesis of ZnO/GNR nanocomposite are shown in the schematic. During the ZnO synthesis, LGONR gets reduced and we named it as GNR.

2.1.3 Electrode Preparation and Supercapacitor Device Fabrication

Typically, 5.0 mg of the powdered sample was ultrasonically mixed with 5 wt % Nafion binder. Formed suspension was sprayed onto 1 cm^2 surface of polished graphite plates. Finally, the deposited films were dried in vacuum oven at 80°C for 24 hrs. The weight of the active material loaded over polished graphite plates was estimated to be 0.25-0.30 mg cm^{-2}. The supercapacitor devices were fabricated with two spray deposited films using Nafion membrane as separator.

2.2 Characterization

Micro-structural features of the electrode materials were recorded through Zeiss Ultra 55 field emission scanning electron microscope (FESEM) and Phillips Technai T-300 high resolution transmission electron microscope (HRTEM). X-ray diffraction (XRD) patterns were recorded on D8 DISCOVER high resolution X-ray diffractometer. X-ray photoelectron spectroscopy (XPS) was done using Perkin-Elmer (model 125) XPS spectrometer. Raman spectroscopy was performed using Renishaw Invia Reflux Micro Raman spectrometer. Brunauer-Emmett-Teller (BET) surface area and Barrett-Joyner-Halenda (BJH) pore size measurement were performed on Micromeritics ASAP 2020. Electrochemical characterizations were carried out in 0.5 M Na_2SO_4 using three electrode cell assembly with Pt sheet as counter, Ag/AgCl as reference and the spray-coated films as working electrode. Cyclic voltammetry (CV) and electrochemical impedance spectroscopy (EIS) were performed by CHI 604 D electrochemical workstation. EIS studies of electrodes were done in frequency range 10 mHz-100 kHz at an amplitude of 5 mV. Galvanostatic charge-discharge (GCD) measurements were carried out at different current densities with Potentiostat Galvanostat EIS Analyzer PARSTAT 4000. Estimation of the supercapacitor device attributes like energy/power density was undertaken through the GCD curves using following equations.[34]

$$C_m = \frac{I \times \Delta t}{m \times \Delta V} \quad (1)$$

$$C_{sp} = 4 \times C_m \quad (2)$$

$$E = \frac{1 \times C_m \times \Delta V^2}{2 \times 3.6} \quad (3)$$

$$P = \frac{3600 \times E}{\Delta t} \quad (4)$$

Here, C_m is supercapacitor device capacitance determined in F g^{-1}, C_{sp} is the specific capacitance of electrode measured in F g^{-1}, i refers to current density in mA cm^{-2}, ΔV is the potential window after IR-drop, m is the active mass loading on electrodes in mg, Δt is discharge time after IR-drop, E is energy density in terms of Wh kg^{-1} and P is power density in W kg^{-1}.

3. RESULTS AND DISCUSSION

Stepwise illustration for the formation of ZnO/GNR nanocomposite is depicted in Fig. 1. MWCNTs are chemically unzipped to form LGONR wherein the holes are created in lacey pattern. Growth of ZnO particles takes place on the edges of the holes (defects) of nanoribbons through co-precipitation method followed by heat treatment at 250ºC during which CO_2 evolves and ZnO is formed.

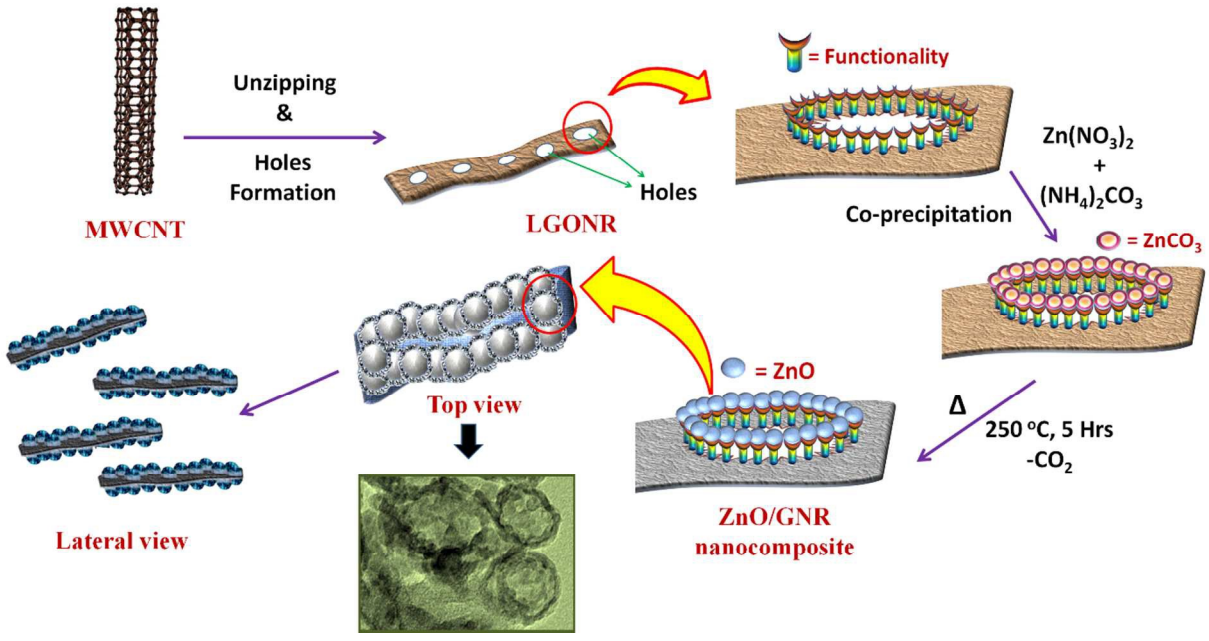

Fig. 1 Schematic for formation of ZnO/GNR nanocomposite.

3.1 Microstructural Investigations

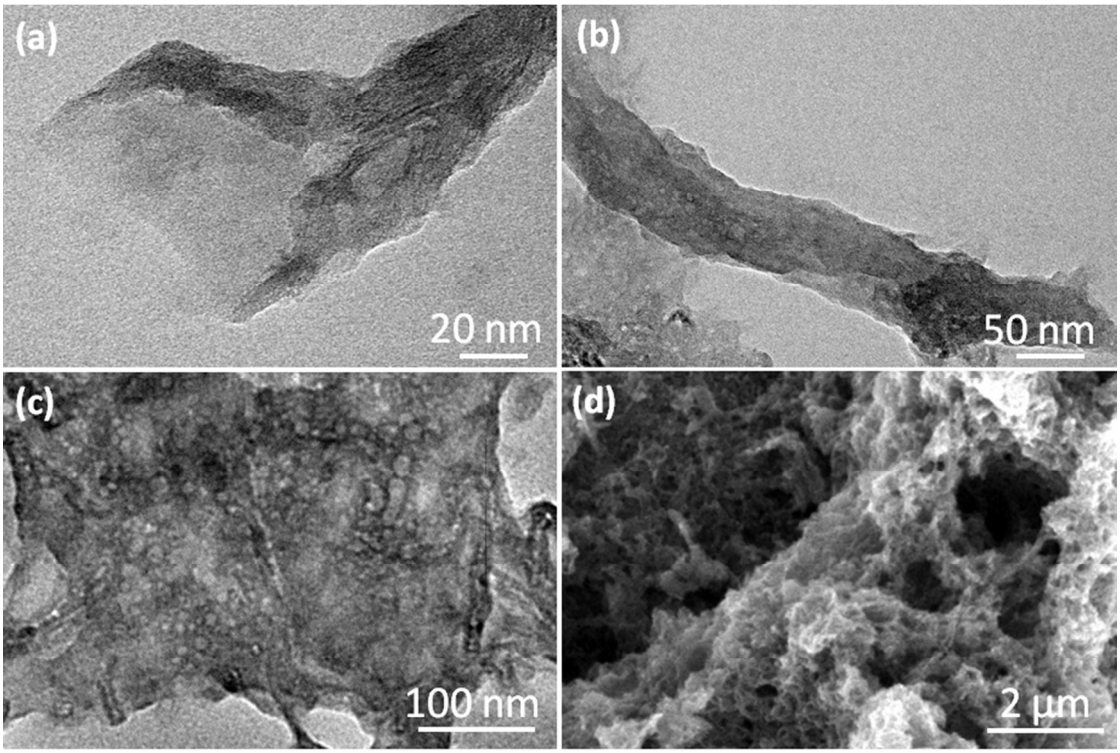

Fig. 2(a) HRTEM of a MWCNT depicting the terminal opening of a nanotube, (b) HRTEM of LGONR indicating complete opening, (c) HRTEM of LGONR showing large area distribution and (d) FESEM image of LRGONR spray coated electrode.

The morphological details of ZnO and GNR in the ZNO/GNR nanocomposite are explicitly described by the microscopic study presented in Fig. 2-4. Fig. 2a shows the HRTEM image of semi-opened MWCNT obtained immediately after the complete addition of $KMnO_4$ during the synthesis. The image clearly reveals longitudinal opening and subsequent formation of holes in MWCNT. Completely opened MWCNT with holes is shown in Fig. 2b. TEM micrograph in Fig. 2c shows the large area distribution of LGONR. These holes located throughout the LGONR promote growth of ZnO nanoparticles owing to the functionalities at edge planes.[35] Fig. 2d

represents the FESEM image of LRGONR electrode indicating entangled arrangement with high mesoporosity.

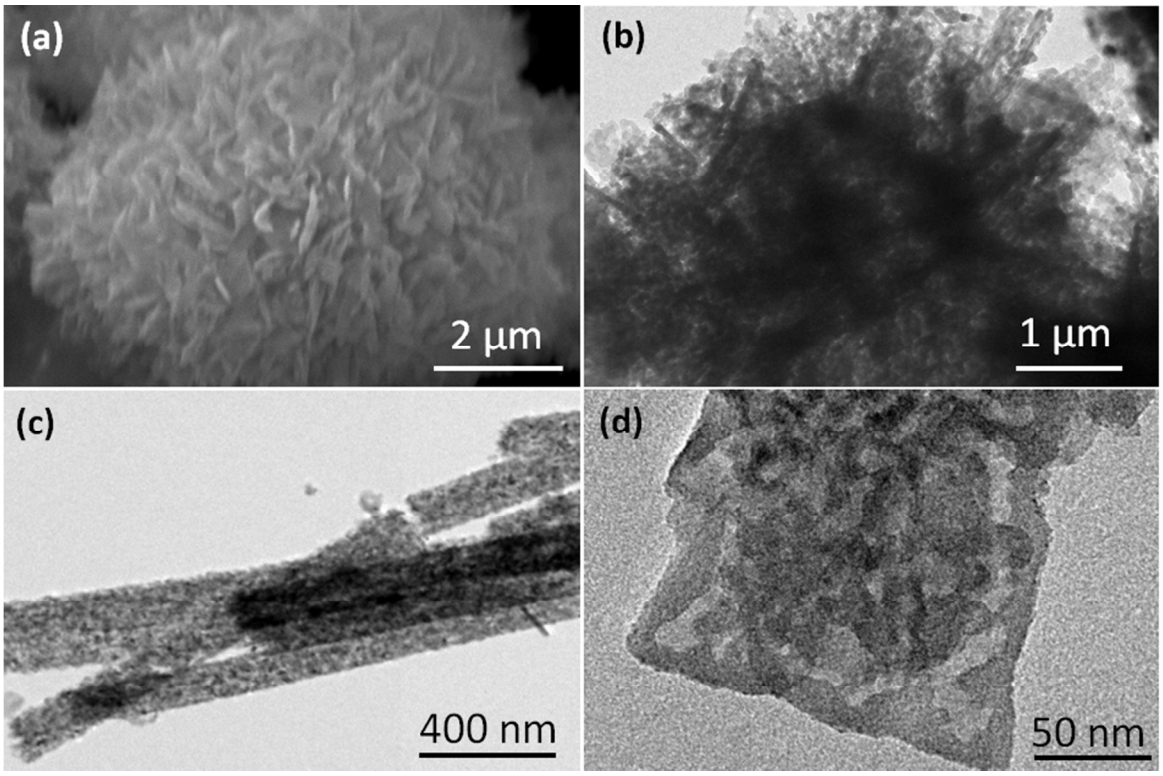

Fig. 3(a,b) FESEM and HRTEM images of ZnO aggregates showing flowery morphology, and (c,d) HRTEM images of ZnO nanorods depicting its morphology.

In contrast ZnO particle growth takes characteristic rod shaped morphology. In current study Fig. 3a and 3b show the FESEM and HRTEM images of ZnO respectively synthesized without GNR support. Herein, the ZnO particles appear agglomerated and form flower-like clusters. Expectantly, the growth of ZnO nanorods occurs in a random order and due to van der Waal attractions these attain a circular flowery morphology.

The HRTEM images for pure ZnO observed at higher magnification are given in Fig. 3(c, d). Evidently, the ZnO growth attains rod shape structure with lengths ranging from 1-2.5 µm

and diameter 150-200 nm (Fig. 3c). Morphological details of the ZnO rod in Fig. 3d reveal irregular and porous characteristics.

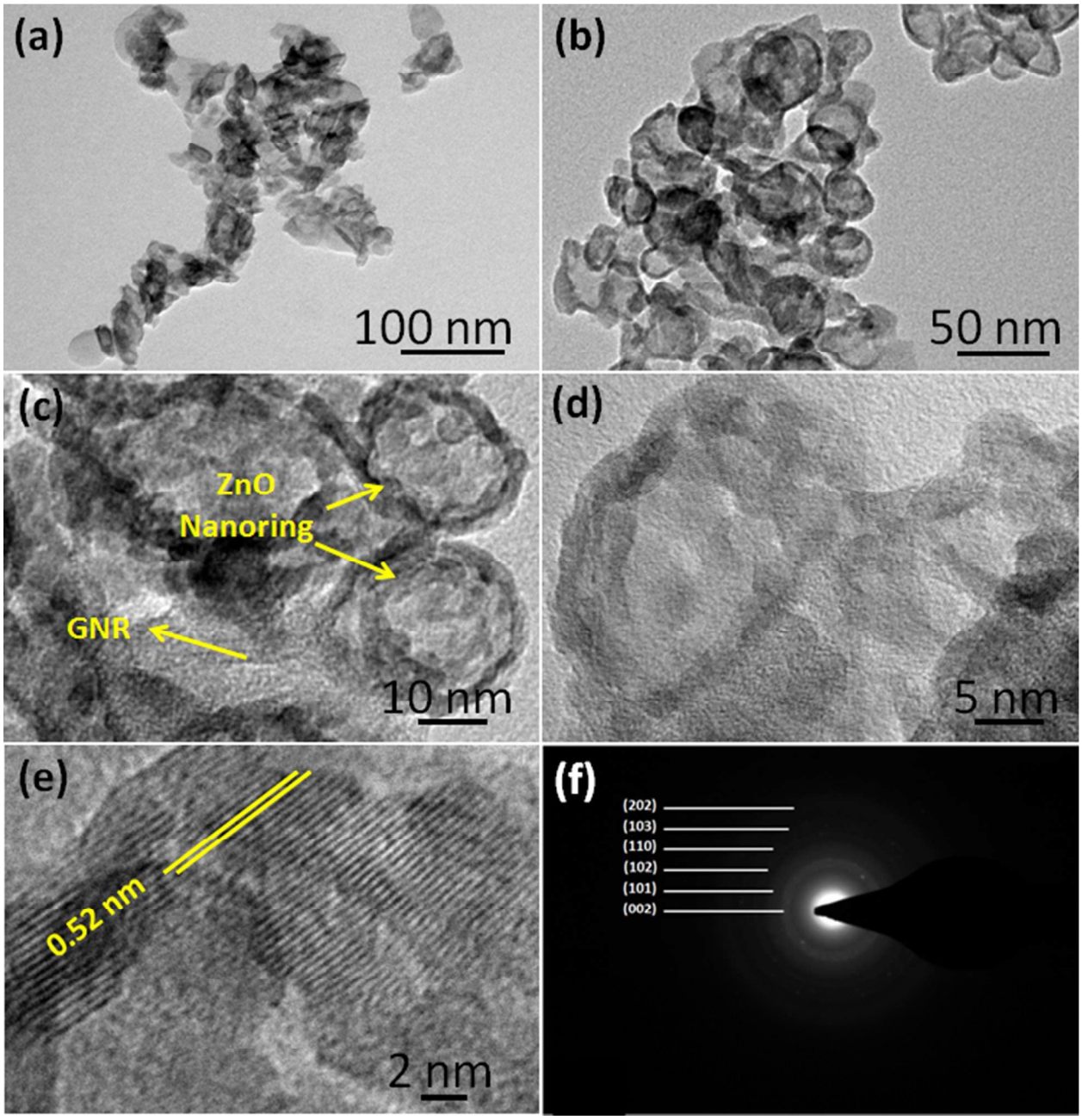

Fig. 4 TEM images of ZnO/GNR nanocomposite indicating (a, b) preferential adsorption of ZnO over GNR, (c) formation of ZnO nanorings over GNR support, (d) HRTEM image shows the orientation of ZnO nanorings over GNR and (e) the ZnO lattice fringes at high magnification, and (f) SAED pattern for ZnO/GNR nanocomposite marked with different planes for ZnO inter-planar spacing.

The TEM micrographs of ZnO/GNR nanocomposite are depicted in Fig. 4(a-e). Significant variations are observed in the micrographs compared to those obtained from ZnO alone, indicating profound influence on the structural characteristics of nano structured composite. The TEM micrograph in Fig. 4a plainly indicates the adsorption of ZnO nanorings over GNR. Unlike the pure ZnO structures (generally rods) which freely grow throughout and acquire large dimensions, the ZnO structures assemble on GNR surface and arise having tiny ring-shaped morphology. This can be attributed to the substrate-assisted growth of ZnO particle assembly limited to the surface of GNR. Fig. 4b gives a closer view of ZnO/GNR nanocomposite. It is examined that ZnO nanoparticles (2-3 nm dia.) join together in a sequential manner forming spiral thread-like structure. It appears that the growing ZnO particles instead taking a rod shape connect together in a spiral form and such thread type morphology of ZnO upon adsorption over GNR form rings over the holes present in GNR. Fig. 4(c, d) confirms the interlinked ZnO nanoring formation over GNR. Fig. 4(c, d) shows that ZnO rings (15-20 nm dia.) completely cover the GNR surface in a manner that the electrolytic accessibility of GNR or ZnO is not hindered. At higher magnification, ZnO/GNR nanocomposite indicates the mesoporous structure (Fig. 4d).

Remarkable finding of this work is that the ZnO/graphene nanocomposites generally exhibit large and irregular shaped ZnO particles.[26,36] However, by the application of a GNR support (~20 wt.%) during growth, ZnO particle dimensions were significantly confined and the ordered adsorption over GNR was achieved.

The lattice fringes shown in Fig. 4e correspond to ZnO. The lattice spacing (2.6 Å) in agreement to the XRD results (discussed in next section), confirm the presence of (002) plane of

ZnO (Wurtzite-type crystal) in nanocomposite. Fig. 4f shows the SAED pattern of ZnO/GNR suggesting its polycrystalline nature.

3.2 Structure Identification

(a) X-ray Diffraction

Fig. 5a shows the XRD patterns of ZnO, LGONR and ZnO/GNR nanocomposite. The diffraction study reflects upon the crystallographic properties of ZnO and ZnO/GNR nanocomposite together with the extent of LGONR oxidation. In figure, the diffraction curve of LGONR shows two crystalline peaks at $2\theta = 9.8^{o}$ and 43.5^{o} ascribed to (002) and (100) plane respectively. The presence of (002) plane indicates high oxidation level in graphene oxide nanoribbons which is further verified by XPS (Figure S1, Supporting Information).[29,33] The sharp peaks are observed for pure ZnO at $2\theta = 31.7^{o}$, 34.5^{o}, 36.2^{o}, 47.4^{o}, 56.8^{o}, 62.8^{o}, 66.3^{o}, 67.9^{o}, 69.1^{o} corresponding to (100), (002), (101), (102), (110), (103), (200), (112) and (201) crystal planes respectively.

Interestingly, the diffraction pattern suggest absence of secondary phases like $Zn(OH)_2$ in the crystal structure of ZnO. The data correlates with the JCPDS card No.-01-079-2205, indicative of wurtzite structure of ZnO.[26] In contrast, the ZnO/GNR nanocomposite depicts XRD pattern similar to that observed for ZnO but with reduced intensity which can be ascribed to the amorphous nature of underlying GNR. Noticeably, concentric rings for different planes in the SAED pattern of nanocomposite (Fig. 4f) also coincide with the d-spacing observed.

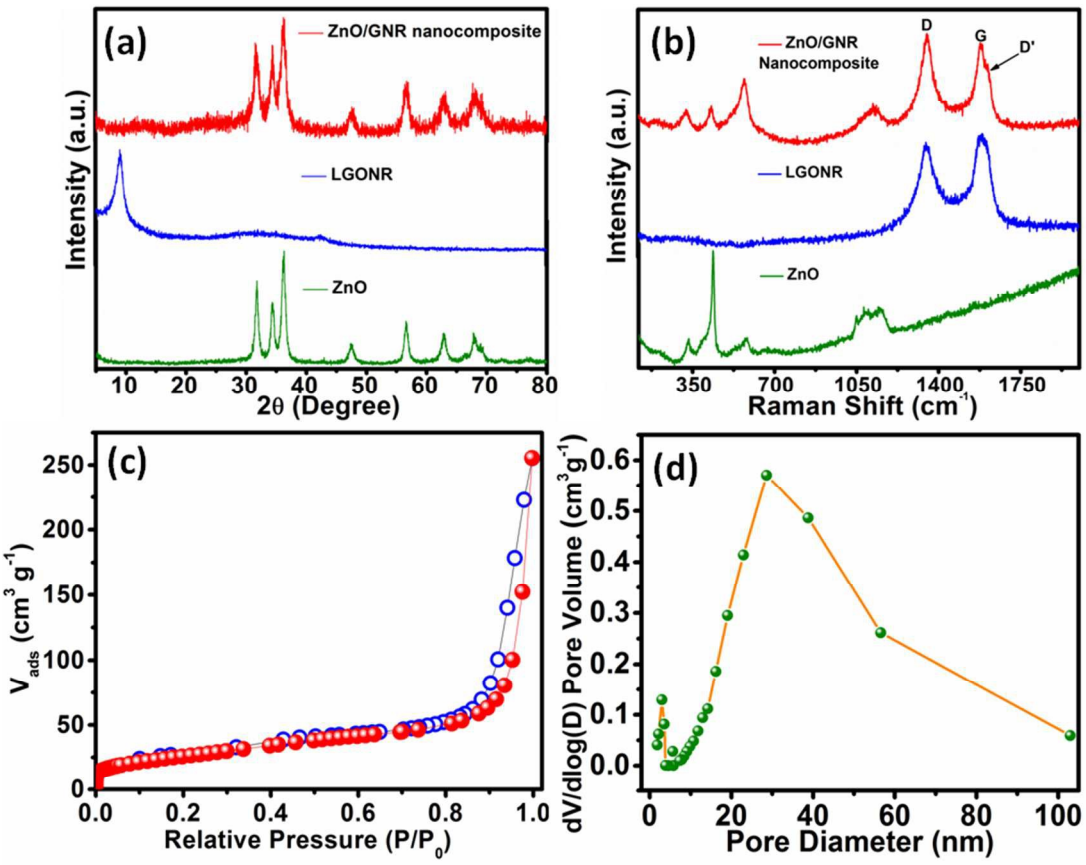

Fig. 5(a) XRD patterns of ZnO, LGONR and ZnO/GNR nanocomposite, (b) Raman spectra of ZnO, LGONR and ZnO/GNR nanocomposite, and (c, d) N_2 adsorption-desorption isotherm and BJH pore size distribution of ZnO/GNR nanocomposite.

(b) Raman Spectroscopy

The Raman spectra of ZnO, LGONR and ZnO/GNR nanocomposite are overlaid in Fig. 5b. The spectrum of ZnO exhibits characteristic peaks at 324 cm^{-1}, 431 cm^{-1}, 568 cm^{-1} and 1102 cm^{-1}.[26] While, the spectrum of LGONR and ZnO/GNR nanocomposite depicts D peak (1370 cm^{-1}) and G peak (1584 cm^{-1}) with intensity ratio (I_D/I_G ratio) 0.92 and 1.07 respectively. The increase in I_D/I_G ratio of ZnO/GNR is attributed to the presence of lattice defect after reduction. High temperature treatment during ZnO/GNR synthesis expels the functionalities of LGONR and

consequently results in defected GNR lattice. The shoulder D′ peak in the G band confirms the existence of lattice defects.[29]

3.3 Specific Surface Area and Pore Size Distribution

The N_2 adsorption-desorption isotherm of ZnO/GNR nanocomposite in Fig. 5c indicates intra and inter particle mesoporosity.[37] BET specific surface area is found to be 92 $m^2 g^{-1}$ which is higher in respect to the ZnO/graphene composite observed in earlier reports.[38-42] Pore size distribution depicted in Fig. 5d using the BJH method, supports the inference isolated from the N_2 isotherm. Maximum pore volumes are occupied by the pores in the range of 2-50 nm with less contribution from the micro and macro porosity.

3.4 Electrochemical Performance

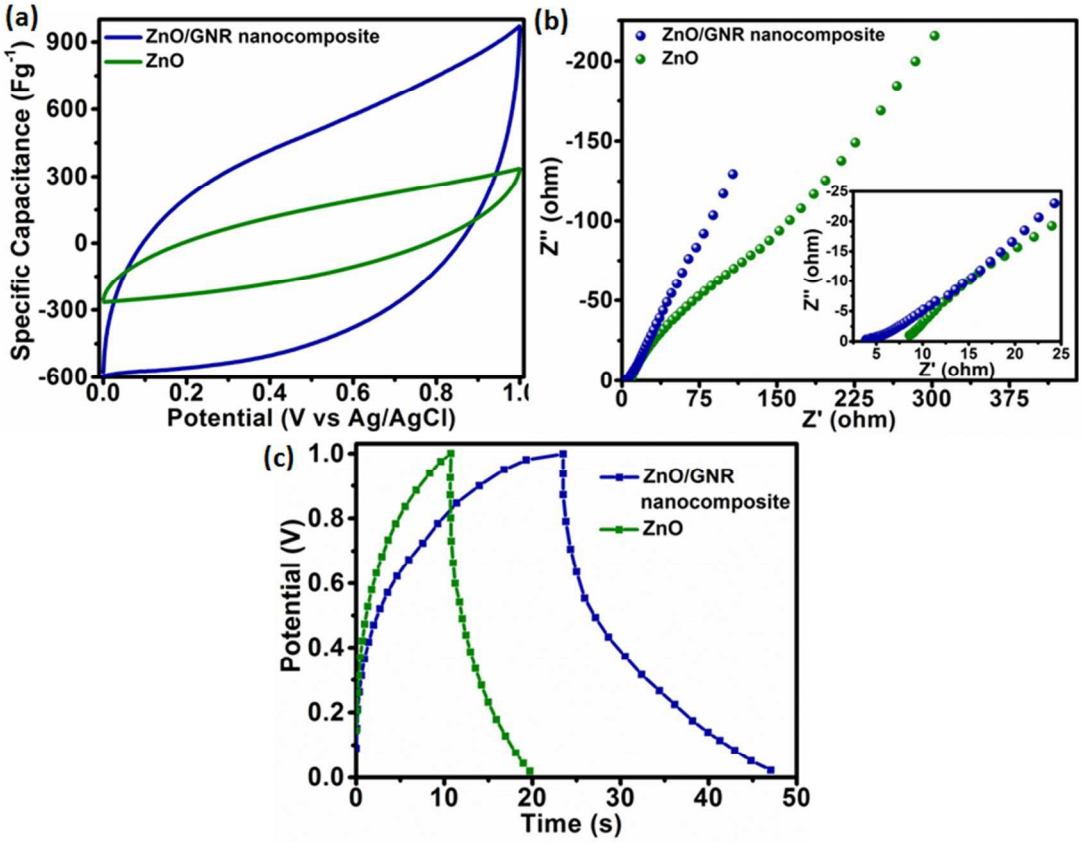

Fig. 6 (a, b) CV and AC impedance curves of pure ZnO and ZnO/GNR nanocomposite, and (c) GCD curves of ZnO/GNR nanocomposite and ZnO at 0.5 mA cm^{-2}.

The electrochemical performance of ZnO and ZnO/GNR nanocomposite electrode was studied in three electrode cell using 0.5M Na_2SO_4 electrolyte as depicted in Fig. 6a. Voltammogram (@5mVs^{-1}) reveals moderate C_{sp} for pure ZnO (161.5 F g^{-1}) and nearly three time higher C_{sp} value for ZnO/GNR nanocomposite electrode (450 F g^{-1}). The enhanced charge storage can be attributed to interconnected nanodimensional ZnO particles which firmly adsorb over lacey GNR. Such an assembly of nanoparticles can effectively transfer the charge to the underlying GNR support that in turn acts as localized current collector for ZnO and transfer the charge to the main current collector through GNR-GNR network. Beside the efficient current collection, ZnO nanorings and the holes in GNR (mesopore dia.) enhance the electrolytic accessibility leading to a synergistic effect in ZnO/GNR electrode.

It may be noted that the C_{sp} value obtained for ZnO/GNR nanocomposites in undertaken study is much higher than those reported earlier for related nanocomposites, for instance, carboxylated graphene-ZnO composite (~238 F g^{-1}),[27] graphene-ZnO composite film (~61.7 F g^{-1}),[28] one-pot ZnO-graphene nanocomposite (~192 F g^{-1}),[30] ZnO nanorods-graphene foam (~400 F g^{-1})[23] and ZnO/rgo composite (~308 F g^{-1}).[26]

Fig. 6b shows the Nyquist plot for ZnO and ZnO/GNR nanocomposite. The intercept of the x-axis at nearly 100 kHz in Nyquist plot is the ESR (electrochemical series resistance) of electrode, which corresponds to the internal ohmic resistance of the electrode material. Interestingly, ZnO/GNR nanocomposite exhibited low ESR value (3.7 Ω) contrary to the high ESR (8.5 Ω) of ZnO alone. Low ESR is further attributed to the ordered ZnO nanostructures adsorbed over lacey and interconnected GNRs with high electrolytic accessibility. The

performance of the supercapacitor devices fabricated from pure ZnO and ZnO/GNR electrodes in symmetric design was analyzed in Fig. 6c. The C_{sp} calculated from GCD of ZnO and ZnO/GNR nanocomposite at 0.5 mA cm^{-2} using equations (1) and (2) reveal much higher C_{sp} value for ZnO/GNR (~125 F g^{-1}) compared to pure ZnO which exhibited merely 30.6 F g^{-1}.

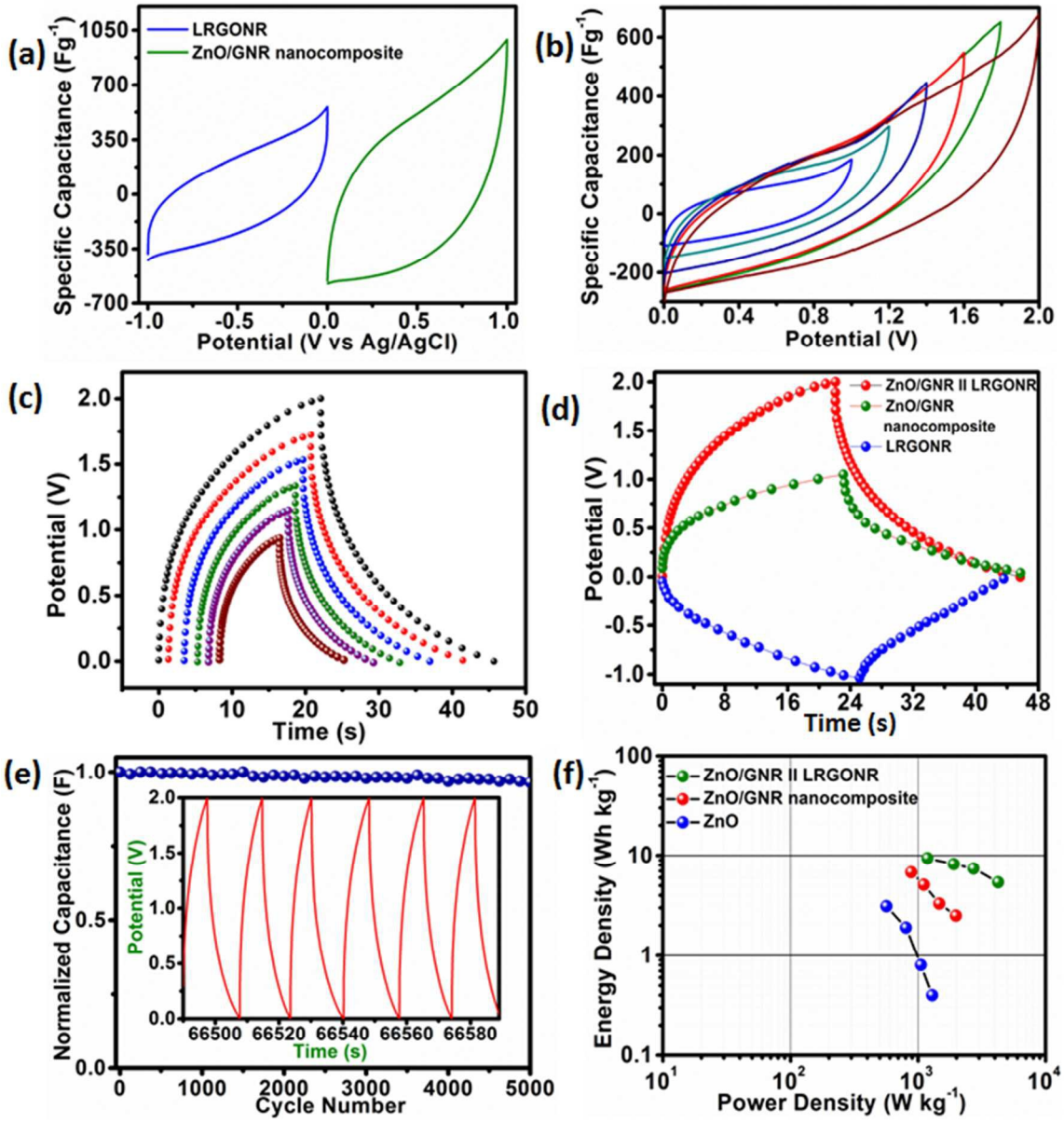

Fig. 7 (a) Three electrode cell CV of LRGONR and ZnO/GNR nanocomposite in best optimized potential window, (b, c) CV (@5 mV s^{-1}) and GCD (@ 0.5 mA cm^{-2}) curves of ZnO/GNR‖LRGONR device in 0.0 V to 2.0 V potential window at an interval of 0.2 V,

(d) comparative GCD characteristics of ZnO (symmetric), ZnO/GNR nanocomposite (symmetric) and ZnO/GNR‖LRGONR (asymmetric) (@0.5 mA cm^{-2}), (e) cycling life of ZnO/GNR‖LRGONR device at 2 mA cm^{-2}; inset showing few segments of GCD during cycling, and (f) Ragone plot showing energy and power density of the proposed devices.

Fig. 7 (a-e) displays the CV and the GCD characteristics of the ZnO/GNR‖LRGONR supercapacitor. The negative electrode in the proposed supercapacitor device was fabricated through separately synthesized LRGONR.[29] As observed in Fig. 7a, both the electrodes have different range of operating potential. It is assumed that the ZnO/GNR‖LRGONR supercapacitor can combine and utilize the charge storage characteristics of both ZnO/GNR and LRGONR as positive and negative electrodes respectively. The idea is confirmed in Fig. 7b that displayed an extended voltammogram up to 2.0 V for ZnO/GNR‖LRGONR supercapacitor. Prior to the fabrication of ZnO/GNR‖LRGONR supercapacitor, CVs of LRGONR and ZnO/GNR electrodes were recorded in three electrode cell for deciding the maximum working potential of asymmetric supercapacitor (Fig. 7a)[43]. Balancing of the charges on both positive and negative electrodes was carried out from the following equation[18].

$$q\ (C) = C_{sp} \times \Delta V \times m \qquad (5)$$

Here, C_{sp} is specific capacitance, ΔV corresponds to the working potential range of charge discharge process, m is the mass loaded on the electrode. Charge balancing is carried out using eq. (5) by putting the values of positive and negative charges followed by considering the ratio of both as:

$$\frac{q_+^*}{q_-^*} = \frac{m_+}{m_-} = \frac{C_{sp-} \times \Delta V_-}{C_{sp+} \times \Delta V_+} \qquad (6)$$

The weight of active material on both the ZnO/GNR‖LRGONR electrodes was standardized and the optimum mass ratio obtained from the above equation for ZnO/GNR‖LRGONR was set to 1:2.7. Using this optimal mass ratio, ZnO/GNR‖LRGONR supercapacitor was fabricated and its redox characteristics were analyzed through CV and GCD tests in 0.5M Na_2SO_4 electrolyte within 1.0 V to 2.0 V, as shown in Fig. 7b and 7c respectively. As expected, the voltammogram in Fig. 7b evidenced constant increase in capacitance with increasing potential. Likewise, GCD recorded for varying potentials starting from 1.0 V to 2.0 V maintains the ratio of charge/discharge time reflecting good columbic efficiency. Furthermore, the GCD characteristics of LRGONR, ZnO/GNR and ZnO/GNR‖LRGONR cell takes nearly same charge-discharge time compared their symmetric counterparts as depicted in Fig. 7d. Cycling life (up to 5000 cycles) of ZnO/GNR‖LRGONR exhibited high performance with 96.7% capacitance retention at 2 $mAcm^{-2}$ (Fig. 7e). Besides, the energy density of ZnO/GNR‖LRGONR, ZnO/GNR (symmetric) and ZnO (symmetric) supercapacitor cell through equation (3) was deduced as 9.4 Wh kg^{-1}, 6.8 Wh kg^{-1} and 3.1 Wh kg^{-1} at power density of 1187 Wkg^{-1}, 884 W kg^{-1} and 565 W kg^{-1} respectively from equation (4) (Fig. 7f) at 0.5 mA cm^{-2}. It is therefore realized that both energy density and power density of the proposed ZnO/GNR‖LRGONR supercapacitor device is improved compared to symmetric design of the constituents.

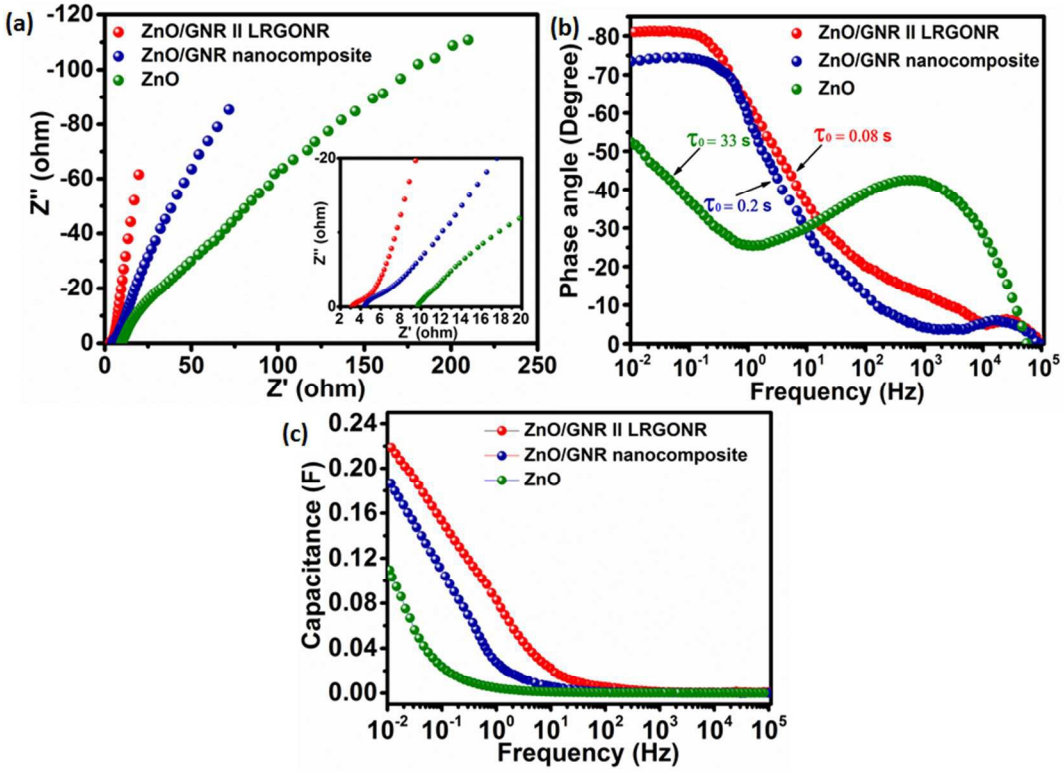

Fig. 8 (a) Nyquist plot of ZnO (symmetric), ZnO/GNR nanocomposite (symmetric) and ZnO/GNR‖LRGONR (asymmetric) devices, (b) Bode plot of the corresponding supercapcitor devices, and (c) variation of capacitance with frequency of the fabricated devices.

The EIS results of the proposed supercapacitors in Fig. 8 show that the ZnO/GNR‖LRGONR supercapacitor exhibited nearly a vertical line parallel to the imaginary axis endorsing highly capacitive character with negligible Warburg resistance (Fig. 8a). However, the symmetric ZnO/GNR and ZnO supercapacitor devices show deviation from the ideal capacitive character owing to diffusion limitations and solution resistance. This is further evidenced by the low ESR value of ZnO/GNR‖LRGONR (3.13 Ω) compared to the symmetric counterparts (i.e. ZnO/GNR ~4.41 Ω and ZnO ~9.6 Ω respectively) which is related to high power output in the supercapacitor device.[44,45] The inset of Fig. 8a further clarifies the improved characteristics of ZnO/GNR‖LRGONR through low R_{CT} value. R_{CT} of the proposed supercapacitors follow the increasing order as ZnO/GNR‖LRGONR (1.19 Ω) < ZnO/GNR (2.67

Ω) < ZnO (15.9 Ω) indicating the improved conductivity through the synergism prevailing between ZnO and GNR.

The Bode lot in Fig. 8b and the capacitance vs. frequency response in Fig. 8c suggest that the ZnO/GNR‖LRGONR device is highly capacitive with phase angle -83^o among the three supercapacitors. Apparently the ZnO/GNR‖LRGONR device (angle -83^o) appears close to the ideal supercapacitor, whereas the ZnO/GNR showed deviation by revealing the phase angle -76^o and ZnO symmetric as -48^o. Relaxation time constant ($\tau_0 = 1/f_0$, f_0 = frequency at -45^o) is an important attribute of the supercapacitor device. τ_0 in case of the ZnO/GNR‖LRGONR cell is found to be 0.08s while the symmetric counterparts showed 0.2s (ZnO/GNR) and 33s (ZnO). Low relaxation time of ZnO/GNR‖LRGONR reflects penetration of ion deeper in the electrode and that the device reached its maximum capacitance with very fast recharging.[46,47] Since ion penetration to deepest layer occurs at low frequency in ZnO symmetric device, its τ_0 value is high. Fig. 8c shows the capacitance response with frequency which is consistent with the relaxation time interpretation. High capacitance is retained in ZnO/GNR‖LRGONR and ZnO/GNR‖ZnO/GNR supercapacitors in a broad frequency region. Capacitance (C) calculation is based on the EIS using the following equation (7)[48]:

$$C\ (\mathrm{F}) = \frac{-1}{2\pi f Z''} \qquad (7)$$

Where, f is frequency and Z'' is the corresponding imaginary resistance.

For the above two supercapacitors, more than 50 % of capacitance is achieved upto 30 Hz which is superior to the ionic liquid based carbon material.[40]

4. CONCLUSIONS

In summary, we report the growth of interconnected ZnO nanorings initiated through functionalities present on the edge planes of lacey graphene nanoribbon (GNR). These nano architectures (ZnO/GNR) were tested in supercapacitor devices. ZnO/GNR nanocomposite electrode exhibits high capacitance (and low resistance) when compared with ZnO synthesized through same procedure without the support LGONR. The enhanced performance is attributed to the reduced size (15-20 nm) and unique ring-like morphology of ZnO on GNR matrix. In contrast to the ZnO/graphene supercapacitors in aqueous electrolytes having short working potential (~1.0 V), the working potential range of ZnO/GNR‖LRGONR was increased up to 2.0 V. The increased potential window resulted in increase (~50 %) of stored energy density from 6.8 Wh kg^{-1} (ZnO/GNR) to 9.4 Wh kg^{-1} (ZnO/GNR‖LRGONR). Furthermore, the relaxation time constant was observed to be two order less in ZnO/GNR nanocomposite (symmetric, 0.2s) and three order less in ZnO/GNR‖LRGONR (0.08s) with respect to ZnO (symmetric, 33s). Likewise, high cycling stability was observed in ZnO/GNR‖LRGONR with up to 96.7 % capacitance retention after 5000 GCD cycle at 2 mA cm^{-2}.

Acknowledgements

The authors gratefully acknowledge University of Delhi for supporting the research through R&D grant (2014-15). Financial support from DST through sponsored research (SR/S1/PC-31/2010) is gratefully acknowledged. One of the authors, V.S. especially acknowledges the SRF award (9/45(1269)/2013-EMR-I) from CSIR, INDIA. Assistance from Inorganic Materials and Catalysis group (Delhi University) for surface area analysis work through N_2 Sorption facility under DST project (SR/S1/PC-11/2011) is also acknowledged.

Note: This work is the part of the thesis of V.S.

References

1. Y. Huang, J. Liang and Y. Chen, *Small,* 2012, **8**, 1805.

2. M.D. Stoller, S. Park, Y. Zhu, J. An and R.S. Rouff, *Nano Lett.*, 2008, **8**, 3498.

3. A.K. Geim and K.S. Novoselov, *Nat. Mater,* 2007, **6**, 183.

4. H.-J. Choi, S.-M. Jung, J.-M. Seo, D.W. Chang, L. Dai and J.-B. Baek, *Nano Energy,* 2012, **1**, 534.

5. K. Kordas, T. Mustonen, G. Toth, H. Jantunen, M. Lajunen, C. Soldano, S. Talapatra, S. Kar, R. Vajtai and P. M. Ajayan, *Small,* 2006, **2**, 1021.

6. V. Subramanian, H. Zhu, R. Vajtai, P. Ajayan and B. Wei, *J. Phys. Chem. B,* 2005, **109**, 20207.

7. A. Rudge, J. Davey, I. Raistrick, S. Gottesfeld and J.P. Ferraris, *J. Power Sources,* 1994, **47**, 89.

8. A. Laforgue, P. Simon, C. Sarrazin and J.F. Fauvarque, *J. Power Sources,* 1999, **80**, 142.

9. L.L. Zhang and X.S. Zhao, *Chem. Soc. Rev.*, 2009, **38**, 2520.

10. G. Wang, L. Zhang and L. Zhang, *J. Chem. Soc. Rev.,* 2012, **41**, 797.

11. K. Naoi, W. Naoi, S. Aoyagi, J.-I. Miyamoto and T. Kamino, *Acc. Chem. Res*., 2012, **46**, 1075.

12. K. Naoi, S. Ishimoto, J.-I. Miyamoto and W. Naoi, *Energy Environ. Sci.,* 2012, **5**, 9363.

13. Z.-S. Wua, G. Zhou, L.-C.Yin, W. Ren, F. Li and H.-M.Cheng, *Nano Energy,* 2012, **1**, 107.

14. G. Yu, X. Xie, L. Pan, Z. Bao and Y. Cui, *Nano Energy,* 2013, **2**, 213.

15. R. Ramya, R. Sivasubramanian and M.V. Sangaranarayanan, *Electrochim. Acta,* 2013, **101**, 109.

16. G.A. Snook, P. Kao and A.S. Best, *J. Power Sources,* 2011, **196**, 1.

17. F. Bonaccorso, L. Colombo, G. Yu, M. Stoller, V. Tozzini, A.C. Ferrari, R.S. Ruoff and V. Pellegrini, *Science,* 2015, **347**,1246501.

18. P. Ahuja, V. Sahu, S.K. Ujjain, R.K. Sharma and G. Singh, *Electrochim. Acta,* 2014, **146**, 429.

19. J. Bae, M.K. Song, Y.J. Park, J.M. Kim, M. Liu and Z.L. Wang, *Angew. Chem. Int. Ed.,* 2011, **50**, 1683.

20. Y. Zhang, H. Li, L. Pan, T. Lu and Z. Sun, *J. Electroanal. Chem.,* 2009, **634**, 68.

21. Y.-B. He, G.-R. Li, Z.-L. Wang, C.-Y. Su and Y.-X. Tong, *Energy Environ. Sci.,* 2011, **4**, 1288.

22. T. Lu, L. Pan, H. Li, G. Zhu, T. Lv, X. Liu, Z. Sun, T. Chen and D.H.C. Chua, *J. Alloys Compd.,* 2011, **509**, 5488.

23. X. Dong, Y. Cao, J. Wang, M.B. Chan-Park, L. Wang, W. Huang and P. Chen, *RSC Adv.,* 2012, **2**, 4364.

24. R.S. Yadav, P. Mishra and A.C. Pandey, *Ultrason. Sonochem.,* 2008, **15**, 863.

25. B. Baruwati, D.K. Kumar and S.V. Manorama, *Sens. Actuators B: Chem.,* 2006, **119**, 676.

26. Y.-L. Chen, Z.-A. Hu, Y.-Q. Chang, H.-W. Wang, Z.-Y. Zhang, Y.-Y. Yang and H.-Y. Wu, *J. Phys. Chem. C,* 2011, **115**, 2563.

27. K.-W. Park and J.H. Jung, *J. Power Sources,* 2012, **199**, 379.

28. T. Lu, Y. Zhang, H. Li, L. Pan, Y. Li, and Z. Sun, *Electrochim. Acta,* 2010, **55**, 4170.

29. V. Sahu, S. Shekhar, R.K. Sharma and G. Singh *ACS Appl. Mater. Interfaces,* 2015, **7**, 3110.

30. Y.-Z. Liu, Y.-F. Li, Y.-G. Yang, Y.-F. Wen and M.-Z. Wang, *Scr. Mater.*, 2013, **68**, 301.

31. J. Bae, Y.J. Park, J.C. Yang, H.W. Kim and D.Y. Kim, *J. Solid State Electrochem.,* 2015, **19***,* 211.

32. E.R. Ezeigwe, M. T.T. Tan, P.S. Khiew and C.W. Siong, *Ceram. Int*., 2015, **41**, 715.

33. D. V. Kosynkin, A. L. Higginbotham, A. Sinitskii, J. R. Lomeda1, A. Dimiev, B. K. Price and J. M. Tour. *Nature*, 2009, **458**, 872.

34. M.D. Stoller and R.S. Ruoff, *Energy Environ. Sci.,* 2010, **3**, 1294.

35. S. Chen, J. Zhu, X. Wu, Q. Han and X. Wang, *ACS Nano,* 2010, **4**, 2822.

36. J. Wang, Z. Gao, Z. Li, B. Wang, Y. Yan, Q. Liu, T. Mann, M. Zhang and Z. Jiang, *J. Solid State Chem.,* 2011, **184**, 1421.

37. C.E. Frey, M. Wiechen and P. Kurz, *Dalton Trans.,* 2014, **43**, 4370.

38. Y.-C. Chena, K.-I. Katsumata, Y.-H. Chiua, K. Okada, N. Matsushita and Y.-J. Hsu, *Appl. Catal. A,* 2015, **490**, 1.

39. A.A. Ashkarran and B. Mohammadi, *Appl. Surf. Sci.,* 2015, **342**, 112.

40. M.K. Kavitha, S.C. Pillai, P. Gopinath and H. John, *J. Environ. Chem. Eng.,* 2015, **3**, 1194.

41. K.B. Babitha, J.J. Matilda, A.P. Mohamed and S. Ananthakumar, *RSC Adv*., 2015, **5**, 50223.

42. Y. Feng, N. Feng, Y. Wei and G. Zhang, *RSC Adv*., 2014, **4**, 7933.

43. S. Grover, S. Goel, V. Sahu, G. Singh and R.K. Sharma, *ACS Sustainable Chem. Eng.,* 2015, **3**, 1460.

44. A. Izadi-Najafabadi, D.T.H. Tan and J.D. Madden, *Synth. Met.,* 2005, **152**, 129.

45. A. Celzard, F. Collas, J.F. Mareche, G. Furdin and I. Rey, *J. Power Sources,* 2002, **108**, 153.

46. L. Zhang, F. Zhang, X. Yang, G. Long, Y. Wu, T. Zhang, K. Leng, Y. Huang, Y. Ma, A. Yu and Y. Chen. *Scientific Reports* 3, Article number: 1408, DOI: 10.1038/srep01408.

47. A. Bello, F. Barzegar, D. Momodu, J. Dangbegnon, F. Taghizadeh, M. Fabiane and N. Manyala, *J. Power Sources,* 2015, **273**, 305.

48. W.-W. Liu, Y.-Q. Feng, X.-B. Yan, J.-T. Chen and Q.-J. Xue, *Adv. Funct. Mater*., 2013, **23**, 4111.